

# 4th HiSST: International Conference on High-Speed Vehicle Science Technology



22-26 September 2025, Tours - France

# **Numerical Analysis on Radiation Effects in Shock Tunnel Experiments**

Chiara Amato<sup>1</sup>, Tim Horchler<sup>1</sup>, Divek Surujhlal<sup>1</sup>, Tobias Ecker<sup>1</sup>, and Giannino Ponchio Camillo<sup>1</sup>

<sup>1</sup>German Aerospace Center (DLR), Institute of Aerodynamics and Flow Technology, Göttingen

#### **Abstract**

This study investigates radiative heat flux contributions in high-enthalpy shock tunnel experiments through a combined experimental and numerical approach. Experiments were conducted in the High Enthalpy Shock Tunnel Göttingen (HEG) using a flat-faced cylinder equipped with heat flux and radiation sensors, while Computational Fluid Dynamics (CFD) simulations were performed with the DLR TAU solver and the next-generation HyperCODA code. Radiation modeling employed both infinite-slab and photon Monte Carlo methods in conjunction with the PARADE database to quantify contributions from shock-layer emission and hot-gas radiation near the nozzle throat. The results indicate that shock-induced radiation accounts for approximately 2% of the convective heat flux at the stagnation point, whereas nozzle-throat contributions are strongly reduced by wall absorption effects and remain of secondary importance. Additional modeling of iron particle radiation suggests that suspended contaminants may dominate radiative heating, potentially explaining the long-observed heat flux anomalies in high-enthalpy facilities. The work confirms the consistency of HyperCODA with TAU for high-enthalpy conditions and highlights the need for further diagnostics of particulate contamination in shock tunnels.

**Keywords:** CFD, hypersonic flow, comparative study, shock tube experiment, radiation investigation

#### **Acronyms**

HyperCODA – Hypersonic CFD for ONERA, DLR, and Airbus
HEG - High Enthalpy Shock Tunnel in Göttingen

Flucs - FLexible Unstructured CFD Software
HIEST - High Enthalpy Shock Tunnel
PARADE - Plasma Radiation Database

#### 1 Introduction

Computational simulations and shock tunnel experiments have been the necessary foundations of hypersonic research. In recent decades, these two approaches have coexisted in synergy, supporting the design of flight vehicles and the study of high-speed, nonequilibrium flows. Their complementary nature defines a powerful framework for hypersonic research where the strengths of one approach can boost the weakness of the other and vice versa. On one side, Computational Fluid Dynamics (CFD) can support the calibration processes of the ground-testing facilities, investigate different aerodynamics configurations, and help in the design of the desired experiment. On the other side, ground testing facilities are necessary to validate the physicochemical numerical modeling and reduce the uncertainty in the prediction of the flow.

This paper aims to make use of the advanced technologies available at DLR from both the experimental and the computational perspectives, and provides a combined effort in analyzing complex aspects of simulating and testing high enthalpy flows. The experiments for this study are performed in the High Enthalpy Shock Tunnel Göttingen (HEG) [1] of the German Aerospace Center (DLR). HEG is a free-piston-driven shock tunnel and is one of the major hypersonic test facilities in Europe. It was designed to investigate high-temperature effects, such as chemical and thermal relaxation, on the aerodynamics of entry or re-entry space vehicles. The computational simulations are performed by using the two in-house CFD codes available: TAU and HyperCODA. TAU [2] is a well-established code capable of accurately solving hypersonic flows, thanks to the spacecraft extension developed since 2010. However, TAU development started more than two decades ago, and adapting it to the newly available hardware to optimize its performance would require a complete redesign of the code structure. Hence, since 2018, ONERA, DLR, and Airbus have focused their efforts on collectively developing a new generation CFD code called CODA (CFD for ONERA, DLR, and Airbus) based on the

structure and design already employed for the solver Flucs (FLexible Unstructured CFD Software) [3]. As it has been done for TAU, DLR has been internally developing an extension for hypersonic applications, HyperCODA [4, 5], that focuses on expanding CODA's physical and numerical modeling capabilities to deal with high enthalpy flows and gas mixtures.

The objective of this analysis focuses on replicating the experimental condition for a flat-cylindrical probe using both codes, and compare the experiment with the CFD predictions. The study concentrates on investigating the different contributions to the surface heat flux, setting up the necessary preliminary CFD testing to support the interpretation of the experimental results. As already shown in previous studies, surface heating measurements in ground testing facilities have shown an overshoot due to uncertain sources. Several theories were proposed during the years such as boundary layer disturbances [6], vibrational excitation [7] and vorticity [8]. Finally, Tanno et al. [9] presented evidence, by carrying out studies in the JAXA's free piston HIEST (High Enthalpy Shock Tunnel) facility, that the heat flux augmentation in high enthalpy facilities was due to radiative processes, since it scaled with the fourth power of the temperature. Furthermore, they conducted an aeroheating test campaign [10] with several blunted models to investigate the actual source of this augmentation. They have shown that the stagnation heat flux was almost three times or higher (based on the analyzed geometry) than the predicted values. Setting a similar experiment to the one used for this study, they demonstrated that the radiation originates from the shock layer ahead of the model. Cruden et al. [11] performed a series of more direct measurements of radiation to the model surface. They conducted experiments on both flat-faced cylinder and an Apollo scaled model using different thermocouples to analyze the radiative nature of the heating augmentation. Furthermore, they compared the experimental results to the simulation solutions obtained with the CFD code DPLR [12]. They have shown that the heat flux augmentation rises when the bow shock reaches the test model. In particular, in the flat-faced cylinder test case, spectroscopy measurements showed impurities within the shock layer with the presence of iron. However, no clear source of this contamination was identified.

Therefore, this study wants to contribute to the investigation of the radiative heat flux contribution in high enthalpy flows by providing a numerical analysis of a radiation probe at HEG condition. The current investigation will take into account the working hypothesis that the excess surface heat flux is caused by two different mechanisms. The first one is gas radiation from the hot expanding gas near the nozzle throat: the gas upstream of the nozzle throat has a very high total temperature and pressure (cf. 1) and is, therefore, expected to radiate thermal radiation. Even when the hot gas expands downstream of the throat, there still might be a significant portion of the nozzle filled with radiating gas. This mechanism has already been investigated before by Oblapenko et al. [13] using a photon Monte-Carlo method for the HEG nozzle also considered here. In this publication, it was also shown that the resulting radiative heat flux on the surface of the measurement probe is very sensitive to optical boundary condition (diffuse vs specular reflection, or even partial absorption) of the nozzle wall. The second mechanism of additional surface heat fluxes due to radiation is caused by gas heating through the detached shock in front of the radiation probe. This contribution to the heat flux anomaly is expected to be lower due to the much smaller radiating gas layer thickness compared to the nozzle near-throat region. However, the radiation probe is equipped with two different radiative heat flux sensors, as shown in Figure 1b and explained in Section 2, the experiments should be able in principle to distinguish between only the shock-induced radiative heat flux contribution and the gas radiation from the nozzle throat.

# 2 Experimental setup in the High Enthalpy Shock Tunnel Göttingen (HEG)

The HEG was commissioned in 1991 for the investigation hypervelocity flow at high stagnation enthalpies up to 23 MJ/kg. It being a free-flying piston-driven shock tunnel means that it is frequently used in the simulation of re-entry and entry flight conditions of up to 60 km altitude at approximately Mach 10 and up to 30 km altitude at approximately Mach 8. More information of the HEG can be found in a recent review of the facility undertaken by the DLR [14].

A critical factor when undertaking high enthalpy investigations in shock tunnels is the measurement of radiation heat flux as a significant part of the total heat flux [10, 6, 15]. Its source is currently hypothesised to originate from flow species and crucially also from contamination species, resulting from entrainment of particulates into the flow in the compression and shock tubes, as well as in the

nozzle throat. This results in contaminant species in the freestream. Although the mass fraction may be small, their radiation in the flow within shock layers can be significant [10, 11].

To address this issue, it was required to systematically investigate the radiation component of heat flux within a shock layer, as well as the possible sources of radiation due to their contribution from flow species and contaminant species. To this end, a flat-faced cylinder test article of diameter 250 mm was tested in the HEG with a reservoir enthalpy of 9.7 MJ/kg and a stagnation pressure of 47.26 MPa. The flat-faced cylinder test object was located 240 mm downstream of the nozzle exit plane [16], equipped for measurements of surface pressure, total heat flux, radiative heat flux and spectral emission within the shock layer. An overview of the test model is shown in figure 1b, in which the orientation and receiving cone angle of the fiber optics for the spectral emission measurements within the shock layer are depicted in green in this figure. In this work, the spectral emission data received by the horizontally-oriented fiber is discussed. Furthermore, the shock standoff distance, measured with a high-speed schlieren optical system will be discussed and compared to numerical simulations of the conditions tested in the HEG.

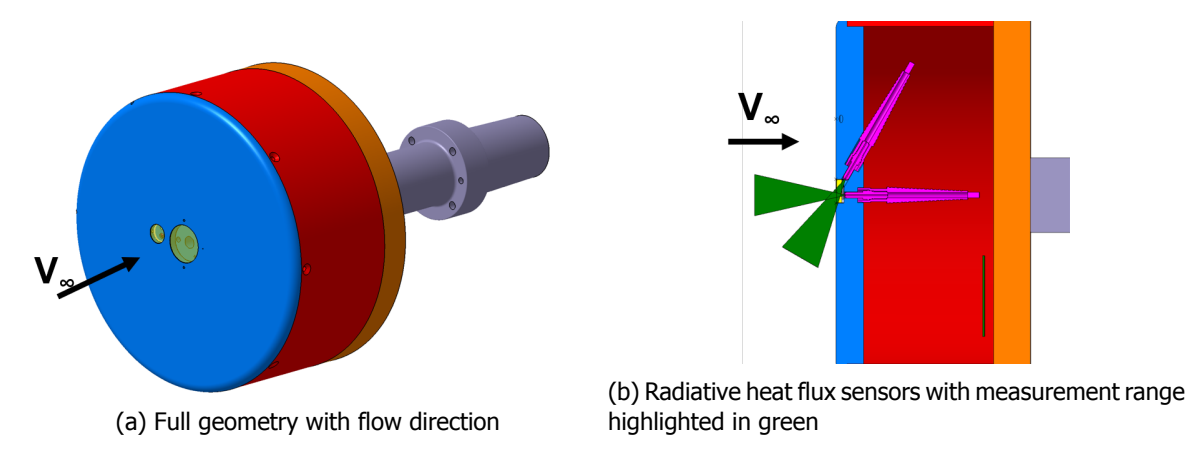


Figure 1: Experiment model

## 3 CFD simulations

The CFD analysis is mainly composed of two steps. First, we simulate an air mixture (76% N<sub>2</sub> and 24% O<sub>2</sub>) flow within the chosen nozzle using the reservoir conditions provided by the facility and summarized in Table 1. The geometry and the mesh of the nozzle is shown in Figure 2 [1].

Table 1: Operating conditions using nozzle 3

Nozzle	Reservoir	p <sub>0</sub> [MPa]	$T_0\left[K\right]$
3	H9.8R2.2	47.26	5912.29

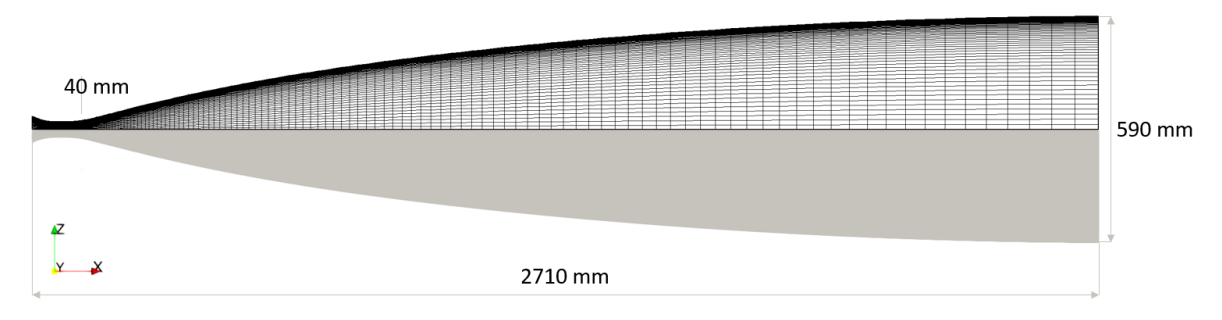


Figure 2: Nozzle 3 geometry and grid

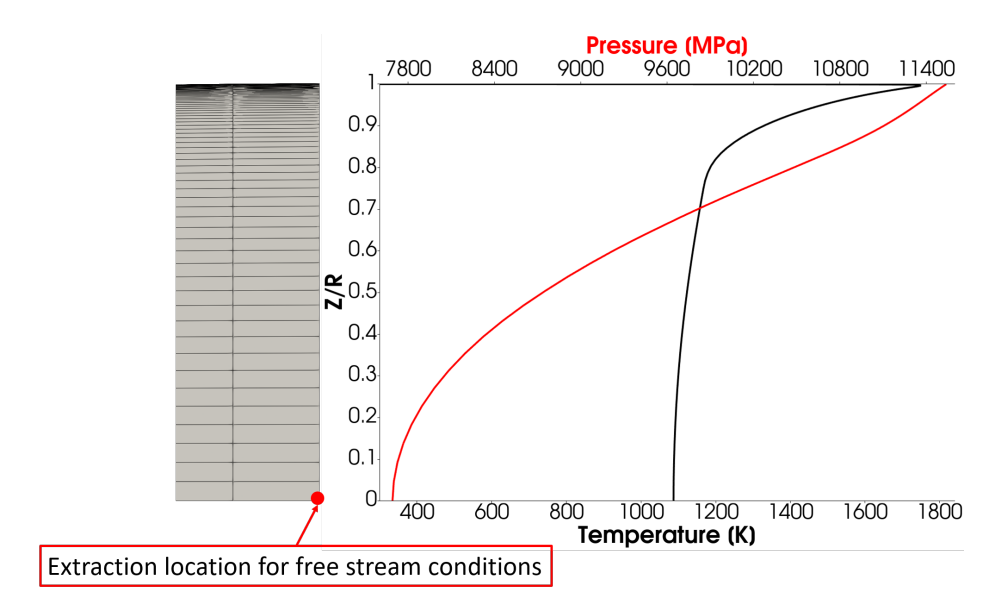


Figure 3: State variable profiles extracted along the exit nozzle.

Figure 3 shows the results extracted along the exit nozzle and plotted with respect to the z coordinates normalized with the nozzle radius. Because the probe is located in the center of the exit nozzle and we simulate half of the domain, we extract the state variables at location highlighted in Figure 3 by the red dot, and use their values as the initial condition for the second part of the CFD study. Consequentially, the radiation probe was simulated in a laminar flow using the free stream conditions summarized in Table 2. The air mixture was represented by a 5 species mixture using the Gupta reaction rates.

Table 2: Free stream conditions for the radiation probe simulation

Mach	6.189
Pressure [Pa]	7688.71
Temperature [K]	1086.604
Density [kg/m <sup>3</sup> ]	0.0242
$Y(N_2)$	0.739857
$Y(O_2)$	0.185307
Y(NO)	0.05814
Y(N)	3.3767e-11
Y(O)	0.01669

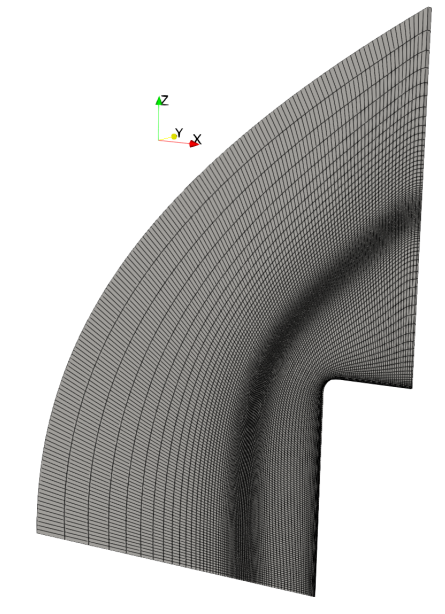


Figure 4: Coarse refined axisymmetric grid

A comprehensive grid convergence study was performed to accurately resolve the flow field. Thus, we built a one-cell wide, one-degree slice of the axisymmetric two-dimensional domain with an offset of  $10^{-8}$  at the origin. Starting with the most coarse grid shown in Figure 4, we varied the first cell wall spacing  $\delta_{\text{wall}}$  and the number of points in both the streamwise and wall-normal directions, doubling up the total number of elements, considering three levels of refinement with three different wall spacing, summarized in Table 3.

We extracted the Mach and the temperature profiles along the stagnation line, and compared the different grid refinements, plotted in Figures 5a and 5b. In these figures, we represent the coarse

Medium **Mesh refinement** Coarse Fine **Number of elements** 39060 156122 626496 Wall spacing 1e-3 1e-5 1e-4 6200 5600 5000 coarse mesh medium mesh fine mesh 3800 3200 2600 -coarse mesh medium mesh fine mesh

2000

1400

800

200

0.02

0.03 0.04 0.05 0.06 0.07 **Distance from the wall (m)** 

(b) Temperature profile

0.08 0.09 0.1

6.0

5.5

5.0

4.5

4.0

3.5 3.0 2.5

2.0

1.5

1.0

0.5

0

0.02

0.03 0.04 0.05 0.06 0.07 **Distance from the wall (m)** 

(a) Mach number profile

Table 3: Summary of the mesh refinements of the 2D domain

Figure 5: Analysis of profiles extracted along the stagnation line for different grid refinements.

0.08 0.09

grid in red, the medium grid in black, and the fine grid in blue. It can be seen that the difference in the prediction of the shock location between the medium and the fine refinement is comparable to the difference of the cell size between the two refinements, and therefore negligible.

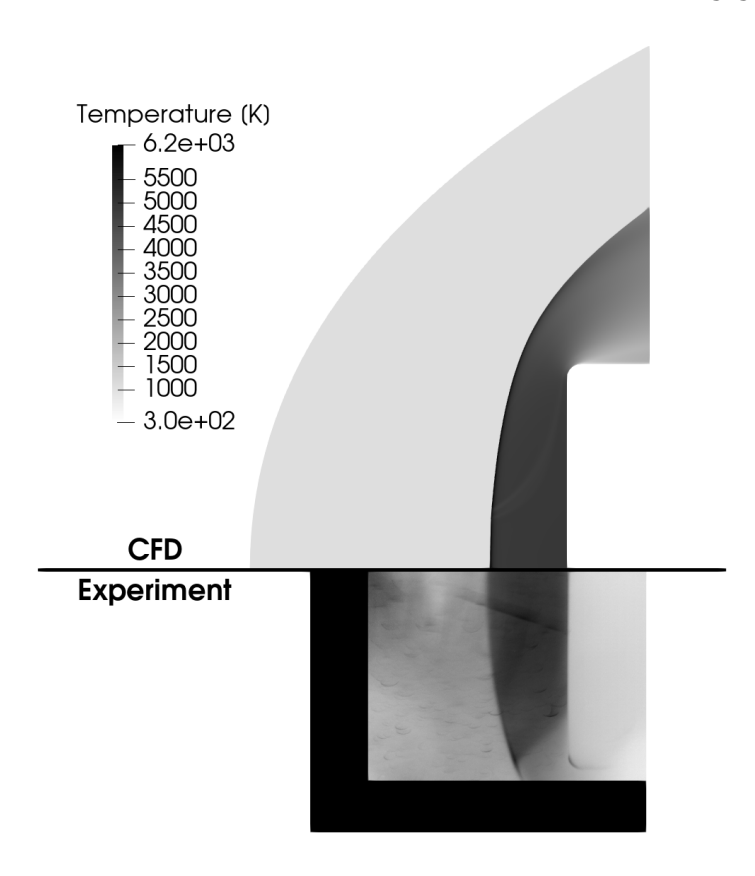
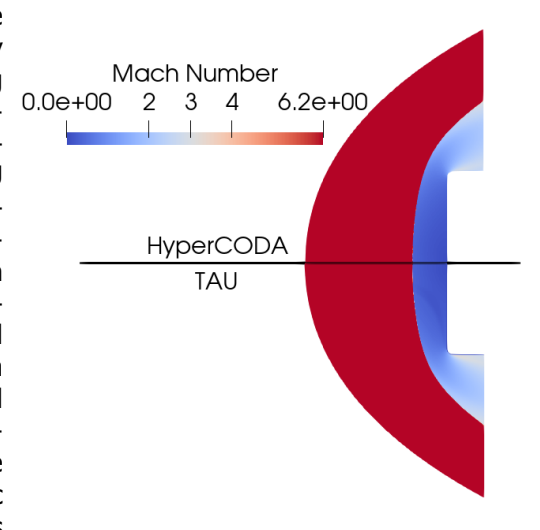


Figure 6: Comparison of the shock standoff distance between the CFD and the experiment results.

The predicted shock standoff distance by the CFD simulations is of 47.1 mm. The shock in the experiment is located at 50.8 mm  $\pm$  1 mm, which differs from the simulation by around 7%. Figure 6 shows the temperature distribution in the flow field predicted by the CFD simulation (on the top) with the schlieren took during the experiment (on the bottom), where the shock location comparison can be seen.

## 3.1 Code validation through code-to-code comparison

One of the aims of this study is to continue the investigation started by Amato et al. in [17] by exploring HyperCODA capabilities, and assessing computational requirements and efficiency in handling high enthalpy flows. Therefore, we performed a code-to-code comparison between TAU and HyperCODA, using the medium refined axisymmetric grid. We are setting the codes using the same PDE (Navier-Stokes), convection scheme (AUSM+M), gas model (ideal gas), reaction mechanism and reconstruction method (2nd order Green-Gauss reconstruction) to ensure a consistent comparison. We should keep in mind that the two codes use different spatial discretizations: HyperCODA is a cell-centered finite volume code, and TAU uses a cell vertex with a dual metric spatial discretization. Hence, some discrepancies are to be expected. In Figure 7, we compare the Figure 7: Comparison of the Mach contour plot Mach number contour plot of the HyperCODA (on between HyperCODA (on the top) and TAU (on the top) and the TAU (on the bottom) solutions.



the bottom)

Furthermore, we compared the temperature and the mass fractions profiles extracted along the stagnation line, portrayed respectively in Figs. 8a and 8b.

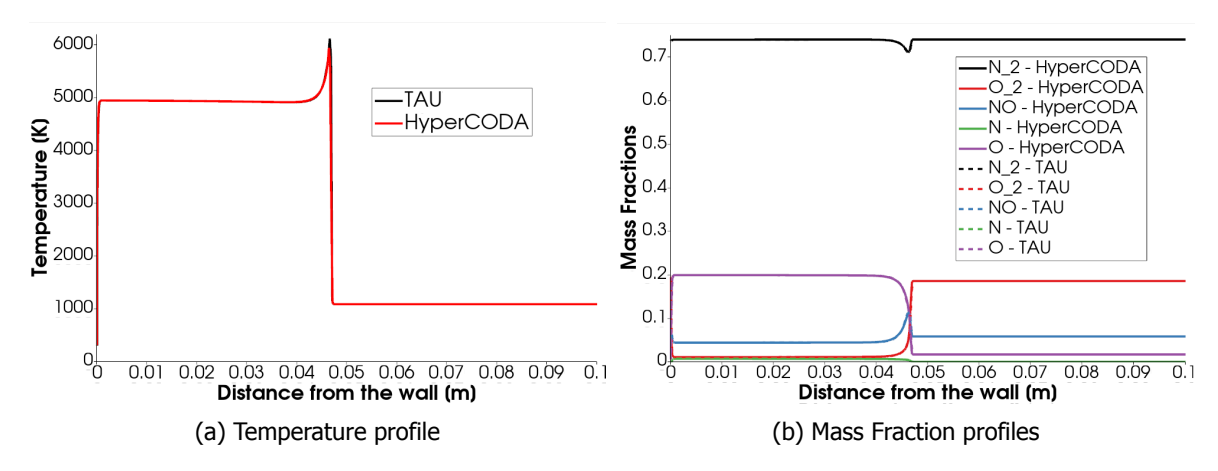


Figure 8: Comparison of profiles along the stagnation line obtained with the different CFD codes.

In Figure 8a, the TAU results are shown in black, and the HyperCODA results in red. In Figure 8b, the TAU results are shown with the dash lines, and the HyperCODA results with the solid lines. The comparison shows almost an exact agreement between the solutions. As mentioned previously, the discrepancies in the temperature profile located at the shock are due to the differences in the spatial discretization between the two codes.

### **Radiation simulation**

The methodology of estimating the radiative heat fluxes will be explained further in this section of the paper. We use the flow field variables temperature and number density from the CFD solutions of TAU and HyperCODA as input for the calculation of all emission  $\varepsilon_\lambda$  and absorption  $\alpha_\lambda$  spectra of the gas. The spectral coefficients are calculated using the third-party software Plasma Radiation Database PARADE (from Fluid Gravity Engineering Ltd.) in Version 2.3. PARADE models three types of radiation mechanism that contribute to radiative heat fluxes: bound-bound transitions, bound-free transitions and free-free transitions. Depending on the processes, these mechanisms contribute discrete wavelength peaks to the spectrum (e.g. for bound-bound transitions in atoms), multiple closely-spaced transition bands (e.g. for vibrational modes in molecules) or continuous spectra for free-free transitions. We assume thermal equilibrium ( $T_{\rm trans.} = T_{\rm rot.} = T_{\rm vib.}$ ) for all spectra used in this publication.

In this work, different radiative quantities need to be considered and a good overview of the different definitions is given in Potter et al. [18]. The total radiated power from a surface is measured in power/surface area/wavelength and is called the spectral emissive power. This quantity does not have any direction dependance and is therefore unsuitable for describing radiative transfer phenomena in participating media with varying properties. Therefore, one defines the spectral radiative intensity  $I_{\lambda}$  in the units power/surface area/solid angle/wavelength. Using the canonical definition of the solid angle on a unit-hemisphere in polar coordinates, the spectral radiative power passing through an infinitesimal area dA is related to the radiative intensity by

$$\dot{q}_{\lambda} = \int_{0}^{2\pi} \int_{-2\pi}^{2\pi} I(\phi, \theta) \sin(\theta) \cos(\theta) d\phi d\theta$$
 (1)

In participating media without scattering effects, the radiative spectral intensity is connected to the spectral emissive power density  $e_{\lambda}$  and the absorption coefficient  $\alpha_{\lambda}$  by the radiative transfer equation

$$\frac{\mathsf{d}I_{\lambda}(s)}{\mathsf{d}s} + \alpha_{\lambda}(s)I_{\lambda}(s) = \epsilon_{\lambda}(s) \tag{2}$$

The spectral emissive power density is given in power/volume/wavelength/solid angle while the absorption coefficient has the units of inverse length (m $^-$ 1). Under the assumption of local thermal equilibrium, the spectral absorption coefficient  $\alpha_{\lambda}$  and the emission coefficient  $e_{\lambda}$  are related by Planck's blackbody function:

$$\alpha_{\lambda} = \frac{\epsilon_{\lambda}}{B_{\lambda}(T)}$$
 with  $B_{\lambda}(T) = \frac{2hc^2}{\lambda^5} \left[ \exp\left(\frac{hc}{\lambda k_B T}\right) - 1 \right]^{-1}$  (3)

The goal of this section is to estimate the radiative heat load contributions from the two different source mechanism present in hypersonic shock tunnels, namely shock-induced radiative heating in front of the radiation probe and hot gas emission from the near throat region of the nozzle. Both processes are summarized schematically in Fig. 9.

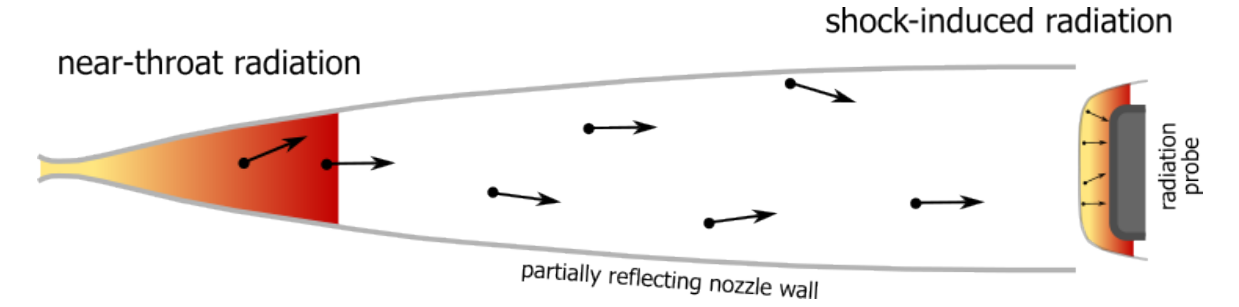


Figure 9: Schematic drawing of the radiative heat loads coming from the nozzle throat region and the shock layer near the radiation probe.

While the additional radiative heat flux induced by the shock in front of the radiation probe can easily be seen in high-speed videos of the test, it has been speculated before, see e.g. [13], that there is an additional contribution from the nozzle reservoir and the near-throat region of the wind tunnel nozzle. Due to the very high temperatures in the nozzle reservoir, there might be an additional significant contribution to the probe radiative heat flux that is usually neglected. In this paper, we will quantify

the amount of radiative heat fluxes from both processes and compare them to the convective heat flux on the radiation probe.

For both mechanisms, different numerical procedures are necessary to integrate the radiative transfer equation 2. The details on the solution process are outlined in the following two sections.

#### Shock-induced radiative heat transfer

For the calculation of the shock-induced radiative heat transfer we employ the infinite-slab model, outlined, for example, in Potter et al. [18]. Due to its flat surface facing the flow, the radiation probe is very well suited for the infinite slab model as almost all variations in flow properties appear perpendicular to probe surface. Near the stagnation point, this will result in a good approximation of the radiative heat flux.

For the infinite slab model, the gas properties parallel to the radiation probe are assumed constant in slabs of finite optical thickness  $\tau_i = \alpha_i \cdot h_i$  with  $h_i$  being the geometrical thickness of slab i: Under

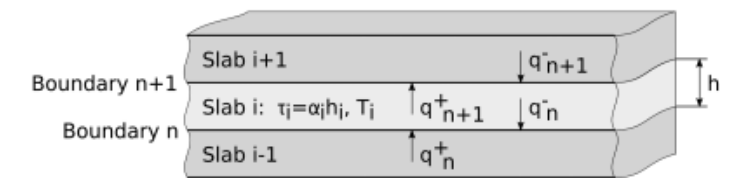


Figure 10: Schematic drawing of an infinite slab model. Image taken from [18].

these assumptions, the radiation heat fluxes at an interfaces of the slab i can be calculated as

$$\dot{q}_{n+1} = \dot{q}_n 2E_3(\tau_i) + \pi \frac{\epsilon}{\alpha} (1 - 2E_3(\tau_i))$$
 (4)

where

$$E_3(\tau) = \int_0^1 \mu \exp(-\tau/\mu) d\mu$$
 (5)

is the exponential-integral equation. Because of its analytical expression, the infinite slab model can also be used to calculate the radiative heat fluxes in a line-by-line approach for each wavelength output of PARADE. By doing so, the infinite slab model automatically takes into account self-absorption within the gas which would be otherwise very prohibitive in terms of computational cost. Balancing the incoming and outgoing fluxes at a given boundary n, the net radiative heat flux is then given as

$$\dot{q}_n = \dot{q}_n^+ - \dot{q}_n^- \tag{6}$$

The incident spectrum on the radiation probe, calculated for the experimental field of view of 12.7 degrees, is shown in Fig. 11. This spectrum is calculated from on the CFD results (temperature and composition number fractions) which are then used as input for PARADE.

The main contribution to the gas radiation heat load results from UV range around 200 nm wavelength. PARADE also calculates the spectrally integrated radiative heat flux to the probe surface by using the infinite slab model.

For the given HEG condition, this results in a radiative heat flux at the stagnation point of

$$\dot{q}_{\text{rad.,shock}} = 86.67 \,\text{kW/m}^2$$
 (line-by-line calculation) (7)

Compared to the convective heat flux on the radiation probe of  $\dot{q}_{\text{conv.}} = 4.42 \, \text{MW/m}^2$ , the shock layer radiation increases the heat load in the stagnation point by about 1.9%.

#### Hot gas emission near the nozzle throat area

Due to the irregular shape of the wind tunnel nozzle, the infinite slab model cannot be applied here. Instead, we will use a photon Monte-Carlo method to calculate the radiative heat component that results from the near-throat radiation. Photon Monte-Carlo methods directly simulate the process of photon propagation by tracing virtual particles through the computational domain. These particles are

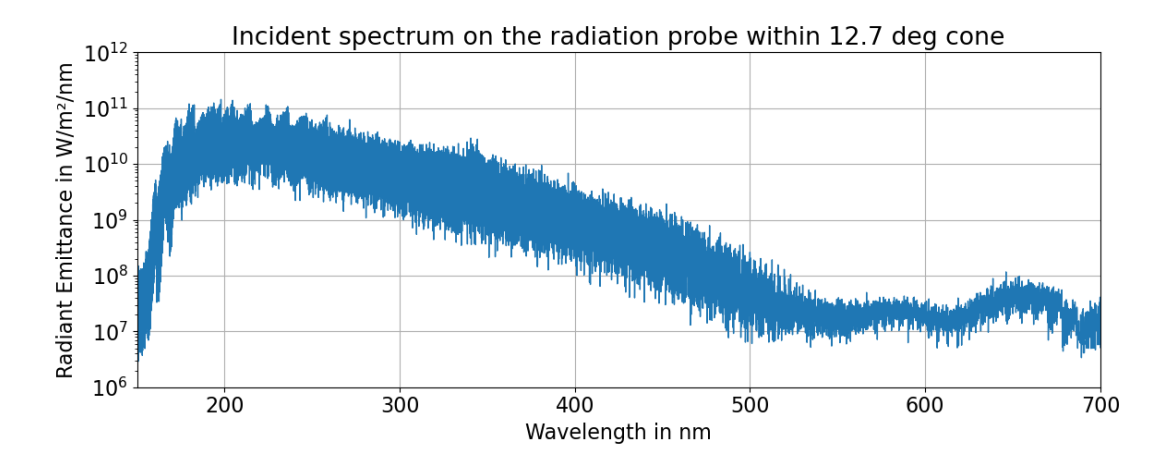


Figure 11: Radiative heating spectrum on the radiation probe.

created at emitting surfaces or within radiating gas layers and carry a fixed amount of energy through the computational domain. Upon creation, these particles are emitted into random directions (based on pseudo-random numbers) covering on a statistical average the true distribution of real photons. The particles are then traced through the domain and are then absorbed, based on a random number statistical criterion on absorbing walls or within the gas volume. Their energy is then deposited at the absorbing wall segment or gas volume. This method is further explained in Karl et al. [19] where it is used to estimate the thermal heat loads from a kerosene rocket plume.

The photon Monte-Carlo method employed here uses a finite-element approach that allows for a simple determination of the flight direction and identification of cell faces where the photon leaves the control volume. Neighbouring cells are also easily found by pre-computed lookup table. Photon Monte-Carlo methods are suitable for complex geometries and when the gas itself is emitting and (self-)absorbing. Its disadvantage is the associated statistical noise introduced by the finite number of photons and a high computational cost when are large number of photons (or cells) are required. The photon Monte-Carlo algorithm is schematically outlined here:

- 1. Within each control volume, the emitted power is being distributed over a fixed number of virtual photons. During this step, the power can be distributed in total, i.e. integrated over the whole spectrum, or spectrally resolved. In this way, the photon Monte-Carlo method can account for largely different absorption coefficients that can occur for example near atomic emission lines.
- 2. Each virtual photon is either emitted isotropically into the computational domain (for volume cells) or according to the Lambert-cosine distribution from emitting surfaces.
- 3. Each photon is traced through the computational domain.
- 4. During its flight through the computational domain, the optical distance L covered by the virtual photon is calculated:  $L = \int \alpha ds$ .
- 5. Once the optical distance exceeds the absorption criterion

$$\int \alpha \mathsf{d}s \le -\mathsf{ln}(1 - R_s) \tag{8}$$

the photon is lost and its energy is deposited in the respective control volume. The random absorption criterion is based on the inverse transformation sampling of the uniformly distributed random number  $R_s$  into an exponential distribution.

6. If the virtual photon hits the boundary of the computational domain (e.g. inflow, outflow or solid wall), the photon is either lost, reflected or absorbed and re-emitted.

In case of absorbed and re-emitted photons, their energy is decreased according to the wall absorption coefficient  $\alpha_w=1-\epsilon_w$ :

$$e_{\mathsf{emitted}} = (1 - \epsilon_w)e_{\mathsf{incident}}.$$
 (9)

Due to high computational cost associated with Monte-Carlo methods, it is necessary to use a much coarser radiation mesh compared to one used in the CFD simulations shown in Fig. 2. Additionally, using a coarser mesh reduces the signal-to-noise ratio in the results as more photons are collected per radiation probe surface element. The radiation mesh used in this study is shown in Fig. 12. It consist of 111 points in axial and 9 cells in radial direction. Even though the radial resolution is quite low, this does not pose a problem as we are only interested in the radiative heat load in the stagnation point of the radiation probe.

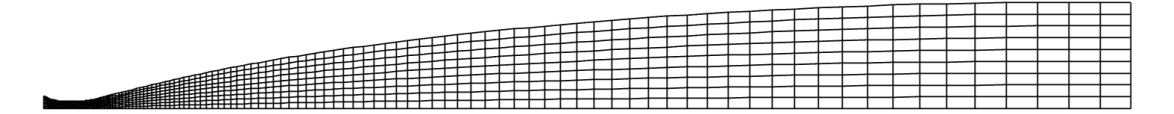


Figure 12: Representation of the coarse radiation grid used in this study.

The problem at hand is axially symmetric, therefore one could also use an axisymmetric reduction of the grid and assume reflecting walls at the sides. However, such functionality is currently not implemented in the photon Monte-Carlo solver. Therefore, we used a full 3D rotated grid for the radiation calculation and averaged the results afterwards in azimuthal direction. Even though this approach is computationally more expensive, it still gives the same noise statistics as the axially symmetric approach due to the spatial averaging in the post-processing step.

We use a 2D axisymmetric TAU calculation (see section on CFD simulations) as input for PARADE to calculate the emission and absorption spectra at each grid point in the nozzle. To further simplify the radiation calculation step, the flow quantities on the nozzle center line are used, therefore making the species mass fractions and the gas temperature distribution a function of the axial coordinate x. This will overestimate the gas temperature as we neglect the cooler boundary layer near the isothermal nozzle wall. The axial distribution of the flow quantities is shown in Fig. 13.

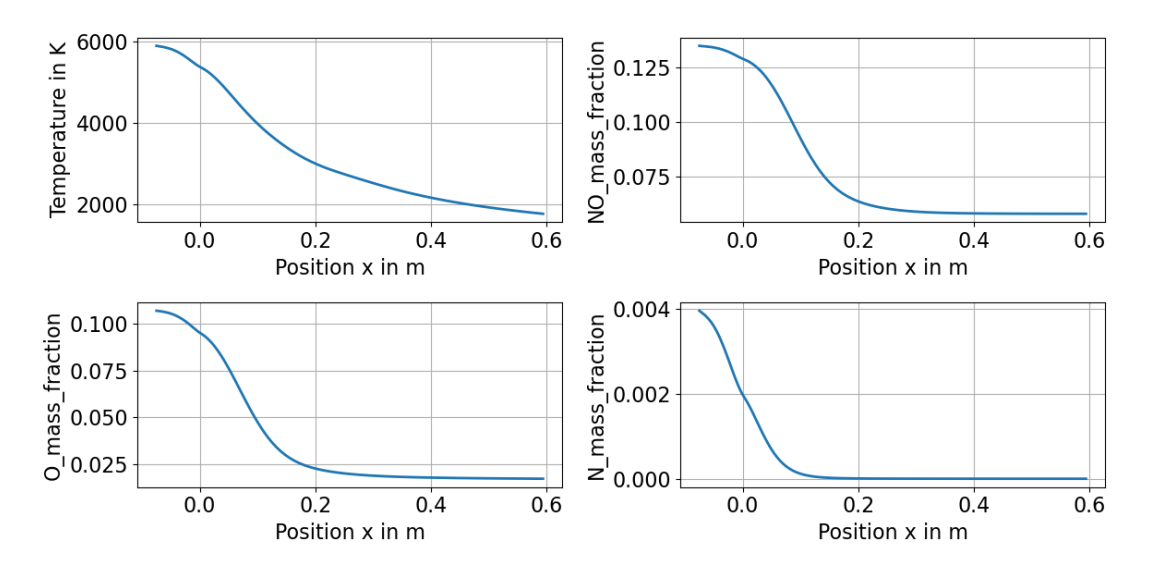


Figure 13: Axial low quantities as input for a PARADE spectrum calculation.

Based on the axial distribution, PARADE calculates the spectrally resolved emission and absorption spectra. As a line-by-line photon Monte-Carlo simulation would be too computationally expensive, it is necessary to spectrally average the absorption and emission spectra. We use the Planck mean which is commonly used to average optically thin spectra. By using the Planck mean, we will overestimate the radiative heat load as the gas is optically thick near the throat.

The mean absorption coefficient is calculated with the Planck mean:

$$\alpha_m = \frac{\int\limits_0^\infty \alpha_\lambda B_\lambda(T) \mathrm{d}\lambda}{\int\limits_0^\infty B_\lambda(T) \mathrm{d}\lambda} \tag{10}$$

From the mean absorption coefficient, we can calculate the corresponding local emission coefficient by

$$\epsilon_m = \int_{0}^{\infty} \alpha_m B_{\lambda}(T) d\lambda = \frac{\alpha_m \sigma T^4}{\pi}$$
 (11)

The axial distribution of these mean absorption and emission coefficients are given in Fig. 14.

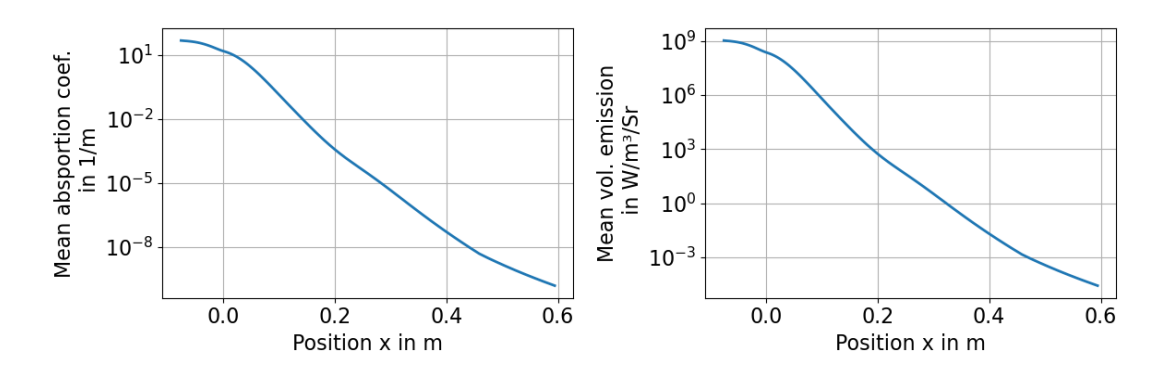
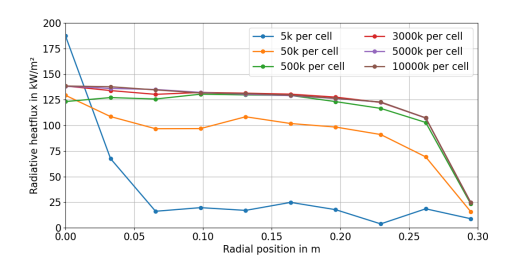


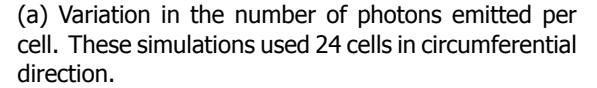
Figure 14: Planck-averaged mean absorption and emission coefficient.

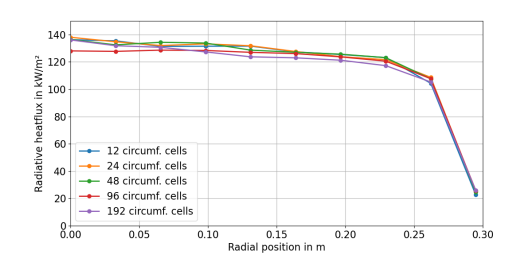
It should be noted that the Planck-mean absorption coefficient upstream of the throat is rather high with a value of  $\alpha\approx 50~\text{m}^{-1}$ , which implies a local mean-free optical path length of  $1/\alpha=0.02~\text{m}$ . This is an indication that the gas is not only strongly emitting in this area but that also self-absorption plays an important role.

In a first step before investigating the sensitivity of the near-throat radiative heat flux to different modelling assumption, we investigated the required number of photons per cell and the influence of the number of cells in circumferential direction. We assumed perfectly reflecting nozzle walls to estimate the maximum possible heat flux on the radiation probe. The influence of the nozzle radiation absorption will investigated later in this section.

The results of this grid and photon statistic convergence study are given in Figs. 15a and 15b.







(b) Solution dependence on the number of circumferential cells for a fixed number of 3 mio. photons per cell.

Figure 15: Grid and photon statistic convergence study

For the first convergence study, we investigated the required number of photons emitted per cell in Fig. 15a. The results show that predicted radiative wall heat flux converges for more than 3 mio. photons emitted per cell.

Fig. 15b shows the result of the grid convergence study where we assessed the required number of circumferential cells. This study shows no clear dependence of the radiative heat flux on the number of circumferential cells used. Previous studies (not shown) indicated that 12 cells might not be enough. We therefore decided to use 24 cells in circumferential direction for all further photon Monte-Carlo investigations.

As mentioned before, the assumption of a perfectly reflecting nozzle wall will certainly overestimate the additional heat flux component to the radiation probe. To investigate the effect of fully absorbing walls ( $\epsilon = 1$ ) vs. partially reflecting and fully reflecting walls ( $\epsilon = 0$ ) are showed in Fig. 16:

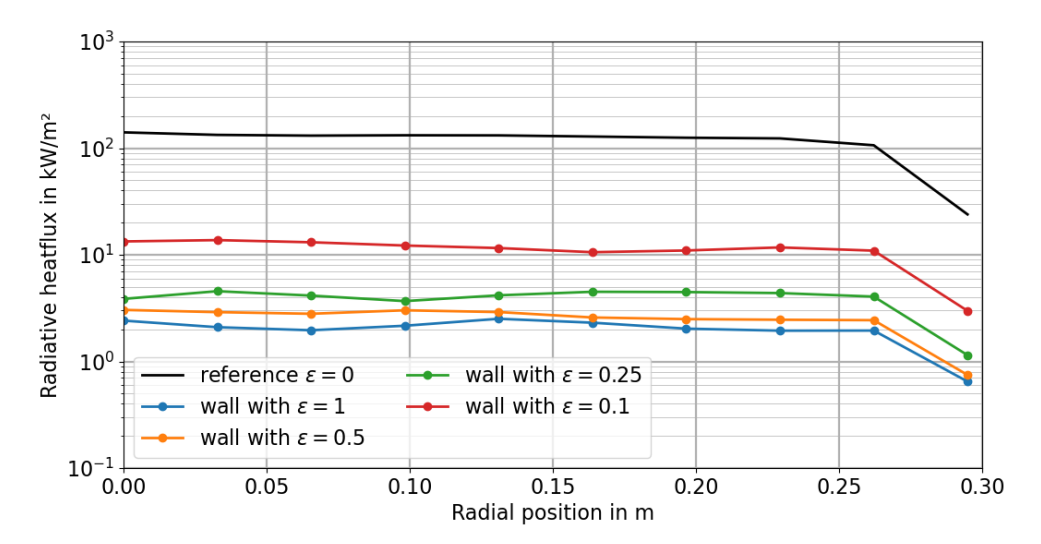


Figure 16: Radiation probe heat flux under the assumption of different wall emission coefficients. All simulations are run at reference conditions with 24 circumferential cells and 3 mio. photons per cell.

Varying the absorption coefficient at the nozzle wall drastically changes the resulting wall heat flux on the radiation probe. Even assuming 90 % reflectivity ( $\epsilon=0.1$ ) reduces the heat flux from the nearthroat region by an order magnitude to approximately 20 kW/m² in the stagnation point. Assuming fully absorbing walls, the radiative heat flux is reduced by almost two orders of magnitude. As the nozzle reservoir and the throat are the regions with the highest gas temperature, we also investigated how much this reservoir contributes to the total heat flux on the radiation probe. For this we manually removed the radiation contribution from the reservoir by assuming to emission and absorption to be zero upstream of the throat (i. e.  $\alpha=\epsilon=0$  for  $x\leq 0$ ).

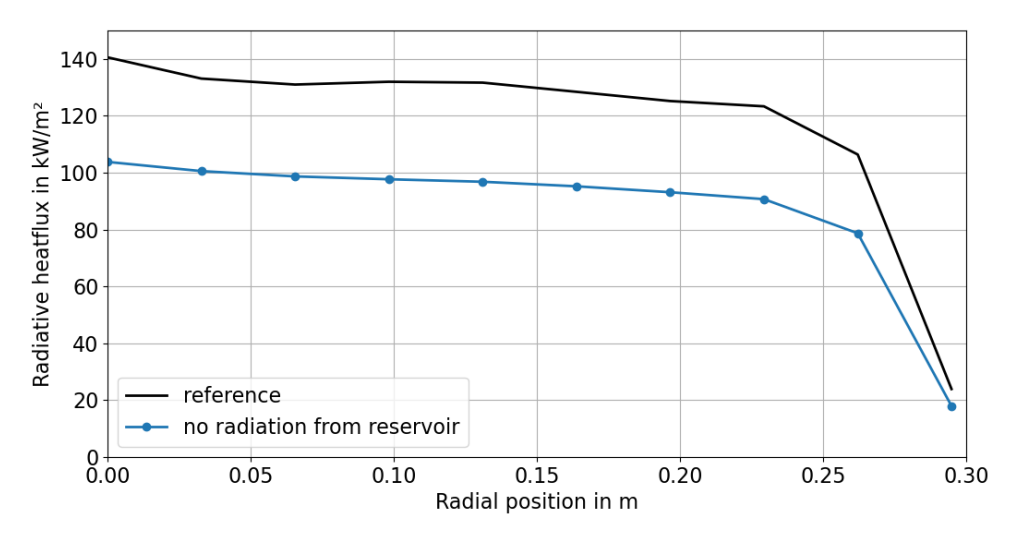


Figure 17: Sensitivity of the radiation probe heat flux towards emission from the reservoir region. All simulations are run at reference conditions with 24 circumferential cells and 3 mio. photons per cell.

Removing radiation from the reservoir reduces the heat flux only by about 35 kW/m². This indicates that self-absorption plays an important role in this area because without self-absorption, a much higher heat flux from the hot gas in the reservoir would reach to the radiation probe surface. This argument is also supported by the high absorption coefficient in this area that suggests an optical mean free path length of about 2 cm. From the perspective of the radiation probe, it can only "see"

about two centimeters into the hot gas near the throat.

These sensitivity studies show that although the radiative heat flux contribution from the hot gas near the nozzle throat is of the same order of magnitude as the shock-layer component, it is unlikely that it contributes significantly to the heat flux anomaly in high-enthalpy facilities. Most of the radiation from the near-throat region is likely to be absorbed by the cold wind tunnel nozzle walls. The small remaining portion of radiating gas with a direct line-of-sight to the radiation probe then only contributes about 2-3 kW/m² to the total heat flux which is not enough to explain the major heat flux increase reported in the literature.

The combined contribution of both the radiating shock-layer and the near-throat region could reach up to 240 kW/m² under most optimal conditions. However, this scenario is not very likely. More realistically, a radiative heat flux from the hot gas can be expected in the range of about 90 kW/m², which is approximately 2 % of the convective heat flux on the probe. Based on the present investigation it is very unlikely that the heat flux anomaly in HEG is caused by gas radiation alone.

# 4.1 Heat flux augmentation from solid particles

The previous investigations in this paper showed that gas radiation is unlikely the source of the heat flux anomaly. Previous work on the heating anomaly (see Cruden et al. [20]) suggest that the additional radiative heat could be caused by contamination from stainless steel (mainly iron, nickel and chromium). This theory is also supported by the operational experience with the HEG which shows contamination on the wind tunnel walls and the models after each test, which requires regular cleaning. The exact composition of these contamination has not been investigated yet in detail. However, for this section of the paper, we want to investigate if blackbody radiation from solid iron particles suspended in the flow can cause a significant contribution to the radiation probe heating. It is speculated that these particles are created during the operation of the piston and the bursting of the diaphragm, and are then carried away by the flow into the test section. We present a simplified model of particle radiation that requires certain assumptions:

ve present a simplified model of particle radiation that requires certain assumption

- 1. We assume solid spherical iron particles with a fixed diameter d
- 2. A fixed amount of iron is contained within the test gas. This results in a nominal iron particle number density
- 3. The iron particles follow the flow, are homogeneously distributed and assume the local gas temperature
- 4. The iron particles are inert, don't evaporate or react in any other way with the surrounding flow
- 5. The particles emit blackbody radiation  $\propto \sigma T^4$

For the iron particle radiation, we assume that the total test gas volume carries 1 g of iron particles homogeneously distributed in particles of size  $d=1\mu\mathrm{m}$ . The test gas volume V is defined as the HEG test time (assume  $T_{\mathrm{test}}=5$  ms) multiplied by the gas free stream velocity at the nozzle exit u=4028 m/s multiplied by the nozzle exit area  $A=\frac{\pi}{4}R_{\mathrm{nozzle}}^2$ :

$$V = \frac{u\pi R_{\text{nozzle}}^2}{4} T_{\text{test}} = 5.506 \,\text{m}^3 \tag{12}$$

The particle number density is then given as the total mass of iron (1 g) divided by the individual mass of each particle, per volume:

$$n_{\rm iron} = \frac{N}{V} = \frac{1}{V} \frac{m_{\rm iron}}{\rho_{\rm iron} \frac{4}{3} \pi \left(\frac{d}{2}\right)^3} = 4.405 \times 10^{10} \, {\rm particles/m}^3 \tag{13}$$

The number density of a species in a mixture of gases is related to the composition  $X_i$  (given in mole fractions) and the total density of the flow  $\rho$  by:

$$n_i = X_i \rho N_A \frac{R_{s,i}}{R_u} \tag{14}$$

where  $N_A$  is Avogadros number,  $R_{s,i}$  is the specific gas constant and  $R_u$  the universal gas constant. Therefore, as long as the composition of the gas mixture doesn't change, the number density is proportional to the total density of the flow. As we assume that iron is an inert species here. Therefore,

its mole fraction  $X_{\text{iron}}$  will not change even when other components of the air are reacting because the total number of moles in air will remain the same. We can therefore assume that the number density of iron is always proportional to the total flow density.

In order to derive the emission and absorption properties of the spherical iron particles, we use the model outlined by Karl et al. [19]. The absorption coefficient is given as the inverse mean free path and the effective particle-cross section by

$$\alpha = \frac{\pi}{4} d^2 n_{\mathsf{iron}}. \tag{15}$$

The particle emissivity is measured in units of W/m<sup>3</sup>/Sr and is given by

$$\epsilon = \frac{1}{4\pi}\sigma T^4 A = \frac{\sigma T^4 d^2}{4} n_{\text{iron}} \tag{16}$$

Based on the flow density and temperature along the stagnation line behind the shock layer, we obtain the following absorption and emission cofficients. In Fig. 18 we compare the Planck-averaged gas radiation data with the emission from the iron particles.

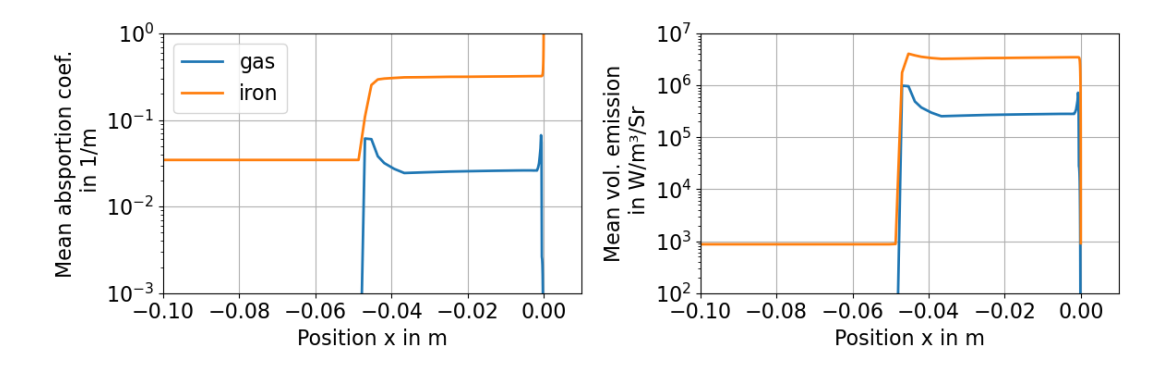


Figure 18: Comparison of the iron emission and absorption coefficient to the gas model results. A particle diameter of 1  $\mu$ m and a total mass of iron particles of 1 g is assumed.

Based on the assumed particle size and total mass deposited in the flow, the emission and absorption coefficients in the shock layer are significantly higher.

These absorption and emission coefficients are then used in the infinite slab model to assess the radiative heat flux from the iron particles on the radiation probe surface. For particles on 1  $\mu$ m diameter and a total of 1 g of iron in the flow, we obtain a radiative heat flux on the radiation probe of

$$\dot{q}_{\text{iron.shock}} = 995.03 \,\text{kW/m}^2 \tag{17}$$

This heat flux contribution is one order of magnitude higher than the radiative heat fluxes from the gas radiation alone. Even though this solid particle model relies on many simplifying assumptions, it still shows that blackbody radiation from suspended particles could potentially be the most relevant source of radiation causing the heat flux anomanly.

In order to investigate the sensitivity of the model, we varied the particle size and the total deposited mass and plotted the corresponding heat flux in Fig. 19.

The sensitivity study shows that the radiative heat drastically changes with change in particle size or total deposited mass. With the chosen combination of 1  $\mu$ m and 1 g, the radiative heat flux from solid particles is approximately the geometric mean of the gas radiation heat flux and the convective heat flux.

For completeness, we also investigated the heat flux contribution from iron particles in the near-throat region. Even though also here, the emission coefficients are significantly higher for the mission from the particles, the total radiative heat flux contribution is only

$$\dot{q}_{\text{iron,throat}} = 116.5 \,\text{kW/m}^2$$
 (18)

when assuming perfectly reflecting nozzle walls. Previous investigations in this work for the gas radiation showed that for a more realistic wall absorption coefficient, the resulting heat flux is of the order of about  $2 \text{ kW/m}^2$ .

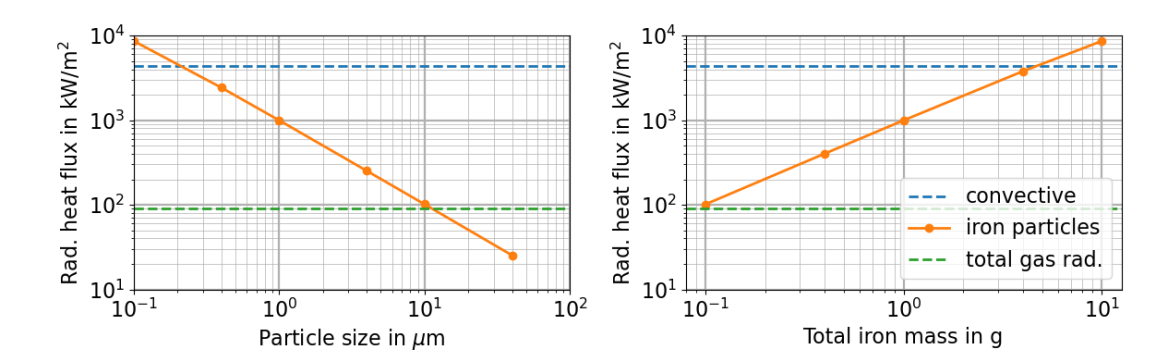


Figure 19: Parametric study on the shock-layer heat flux due to solid iron particles.

Contribution		Heat flux in kW/m <sup>2</sup>	Perc. of convective heatflux
convective		4420	100 %
gas	shock-layer	87	2%
	near-throat max	140	3.1%
	near-throat w absorption	3	0.06 %
	total	90	2 %
particles	shock-layer	995	22.5%
	near-throat max	117	3.1%
	near-throat w absorption	2	0.05 %
	total	997	22.05 %
total radiation		1087	24.6 %

Table 4: Summary of the radiative heat flux contributions

A summary of the different radiative heat flux contributions are given in the following table: We can conclude that the only significant contribution to the heat flux results from solid particle emission in the shock-layer. All contributions from the gas and particle radiation together then account for approximately 25 % of the convective heat flux. We must, however, remark that this number is not exact by any means due to many assumptions made for the simplistic particle radiation model. Later studies need to address the shortcomings of this model in order to obtain more precise results. The conclusion from this study are:

- Gas radiation from the shock-layer and the near-throat region accounts only for an additional two percent of the convective heat load
- While the near throat region also emits radiation at at similar strength as the shock-layer, most of it is absorbed by the nozzle walls
- Radiative heat flux contribution from solid particles in the shock-layer is about an order of magnitude higher than the gas radiation part, based on the given model assumptions.
- The additional heat load from the near-throat region of the nozzle by solid particles is again rather low and also suffers from absorption at the nozzle walls.

## 5 Conclusion and future work

This work presented a combined experimental and numerical investigation of radiative effects in high-enthalpy shock tunnel experiments. Using measurements from a flat-faced cylinder in the HEG facility and CFD predictions with the TAU and HyperCODA solvers, we quantified the contributions of shock-layer and nozzle-throat radiation to the overall surface heat flux. The analysis shows that shock-layer radiation accounts for approximately 2% of the convective heat flux at the stagnation point, while nozzle-throat contributions are strongly attenuated by wall absorption and therefore negligible under realistic conditions. Taken together, these mechanisms cannot explain the large heat flux augmentation consistently reported in high-enthalpy facilities.

Complementary modeling of iron particle radiation demonstrated that blackbody emission from even small quantities of entrained contaminants can produce heat fluxes an order of magnitude higher than gas-phase radiation. This makes particulate radiation a strong candidate for the source of the observed anomaly, in line with previous experimental observations of contamination in HEG. The code-to-code comparison confirms that HyperCODA can reproduce TAU predictions with high fidelity, reinforcing its potential as a next-generation CFD tool for hypersonic applications. Future work will focus on refining the particle radiation model, performing dedicated spectroscopic diagnostics to characterize contaminant species, and coupling radiation solvers more tightly with CFD simulations. Such advances are essential to reduce uncertainty in aeroheating predictions, improve the interpretation of shock tunnel experiments, and increase confidence in the design and qualification of high-speed vehicles.

## **6 Acknowledgements**

The authors gratefully acknowledge the scientific support and HPC resources provided by the German Aerospace Center (DLR). The HPC system CARO is partially funded by "Ministry of Science and Culture of Lower Saxony" and "Federal Ministry for Economic Affairs and Climate Action".

#### References

- [1] Martinez Schramm, J., Wagner, A., Surujhlal, D., and Camillo, G. P., "The High Enthalpy Shock Tunnel Göttingen of the German Aerospace Center (DLR)," Journal of large-scale research facilities JLSRF, Vol. 9, No. 1, 2024.
- [2] Langer, S., Schwöppe, A., and Kroll, N., "The DLR Flow Solver TAU Status and Recent Algorithmic Developments," 2014.
- [3] Leicht, T., Jägersküpper, J., Vollmer, D., Schwöppe, A., Hartmann, R., Fiedler, J., and Schlauch, T., "DLR-Project Digital-X-Next Generation CFD Solver'Flucs'," 2016.
- [4] Huismann, I., Fechter, S., and Leicht, T., "HyperCODA–Extension of Flow Solver CODA to Hypersonic Flows," STAB-Symposium 2020, Vol. 13, 2020.
- [5] Fechter, S. and Huismann, I., "HyperCODA Extension of Flow Solver CODA Towards Rocket Flows," 2022 9th European Conference for Aerospace Sciences (EUCASS), 2022.
- [6] Olejniczak, J., Wright, M., Laurence, S., and Hornung, H., "Computational Modeling of T5 Laminar and Turbulent Heating Data on Blunt Cones, Part 1: Titan Applications," 43rd AIAA Aerospace Sciences Meeting and Exhibit, American Institute of Aeronautics and Astronautics, Jan 2005.
- [7] Hollis, B. R. and Prabhu, D. K., "Assessment of Laminar, Convective Aeroheating Prediction Uncertainties for Mars-Entry Vehicles," Journal of Spacecraft and Rockets, Vol. 50, No. 1, jan 2013, pp. 56–68.
- [8] Marineau, E., Lewis, D., Smith, M., Lafferty, J., White, M., and Amar, A., "Investigation of Hypersonic Laminar Heating Augmentation in the Stagnation Region," 51st AIAA Aerospace Sciences Meeting including the New Horizons Forum and Aerospace Exposition, American Institute of Aeronautics and Astronautics, Jan 2013.
- [9] Tanno, H., Komuro, T., Sato, K., Itoh, K., Takahashi, M., Ishihara, T., Ogino, Y., and Sawada, K., "Heat Flux Anomaly In High-Enthalpy And High-Reynolds Number Flow," 43rd AIAA Thermophysics Conference, 2012, p. 3104.
- [10] Tanno, H., Komuro, T., Lillard, R. P., and Olejniczak, J., "Experimental Study of High-Enthalpy Heat Flux Augmentation in Shock Tunnels," Journal of Thermophysics and Heat Transfer, Vol. 29, No. 4, Oct. 2015, pp. 858–862.
- [11] Cruden, B. A., Tang, C. Y., Olejniczak, J., Amar, A. J., and Tanno, H., "Characterization of radiative heating anomaly in high enthalpy shock tunnels," Experiments in Fluids, Vol. 62, No. 7, June 2021.

- [12] Wright, M. J., White, T., and Mangini, N., "Data parallel line relaxation (DPLR) code user manual: Acadia-version 4.01. 1," Tech. rep., 2009.
- [13] Oblapenko, G., Ecker, T., Fechter, S., Horchler, T., and Karl, S., "Development of a photon Monte Carlo radiative heat transfer solver for CFD applications," 10th EUCASS 9th CEAS 2023, edited by EUCASS and CEAS, Juli 2023, pp. 1–15.
- [14] Martinez Schramm, J., Wagner, A., Surujhlal, D., and Ponchio Camillo, G., "High Enthalpy Shock Tunnel Göttingen of the German Aerospace Center (DLR)," Journal of large-scale research facilities JLSRF, Vol. 9, No. 1, July 2024.
- [15] Collen, P. L. and McGilvray, L. J. D. . M., "Measurements of radiating hypervelocity air shock layers in the T6 free-piston driven shock tube," International Conference on Flight Vehicles, Aerothermodynamics and Re-Entry Missions and Engineering (FAR 2019), 2019.
- [16] Surujhlal, D., Wagner, A., Camillo, G. P., Buntrock, L., Sugarno, I., Gupta, H., and Schramm, J. M., "Radiation of contaminant species in the High Enthalpy Shock Tunnel Göttingen (HEG)," 2024, presented at the 10th International Workshop on Radiation of High Temperature Gases for Space Missions.
- [17] Amato, C., Ecker, T., Horchler, T., Fechter, S., and Huismann, I., "Application of HyperCODA to Hypersonic Flows Around Two-Dimensional Geometries," 3rd International Conference on High-Speed Vehicle Science and Technology (HiSST) 2024, edited by CEAS, CEAS, April 2024.
- [18] Potter, D. F., Karl, S., Lambert, M., and Hannemann, K., "Computation of radiative and convective contributions to Viking afterbody heating," 44th AIAA Thermophysics Conference, 2013, p. 2895.
- [19] Karl, S., Ecker, T., Bykerk, T., Choi, S., and Kim, J., "CFD modeling of soot induced radiation in the exhaust plume of rocket engines," 3rd International Conference on Flight Vehicles, Aerothermodynamics and Re-entry FAR 2025, Mai 2025.
- [20] Cruden, B. A., Tang, C. Y., Olejniczak, J., Amar, A. J., and Tanno, H., "Characterization of radiative heating anomaly in high enthalpy shock tunnels," Experiments in Fluids, Vol. 62, No. 7, 2021, pp. 142.